POLITECNICO
MILANO 1863

SCUOLA DI INGEGNERIA INDUSTRIALE
E DELL'INFORMAZIONE

Efficient Direct Numerical Simulations of Straight and Sinusoidal Riblets in Turbulent Channel Flows

Tesi di Laurea Magistrale in
Aeronautical Engineering - Ingegneria Aeronautica

Stefano Cipelli, 966491

Advisor:
Prof. Maurizio Quadrio

Co-advisors:
Dr.-Ing. Davide Gatti

Academic year:
2021-2022

Abstract: The present thesis presents a finite-difference Direct Numerical Simulation (DNS) code designed to assess the turbulent drag reduction produced by riblets of arbitrary shape. The code's strength lies in its efficiency, achieved through the implementation of an immersed boundary method that incorporates a corner correction for the riblets' edges. The idea hinges on the observation that, near geometrical singularities, convection terms are negligible: the analytical steady Stokes solution is used to correct the immersed boundary terms. As a result, extremely fine grids are not required to properly resolve the riblet tip. The computationally efficient code enabled a comprehensive parametric study, in which longitudinally straight and sinusoidal triangular riblets with a 60-degree tip angle were tested for a wide range of riblet sizes to measure the drag reduction curve. The corner correction was found to be crucial in properly computing both the laminar and turbulent solutions. Results are presented in terms of the friction coefficient and shift in the mean velocity profile. Additionally, results for turbulence statistics such as Reynolds stresses, mean velocity profiles, and Quasi-Streamwise-Vortices position and intensity are also provided. The study focuses particularly on the advantages that sinusoidal riblets provide in comparison to their straight counterparts.

Key-words: Turbulence, Drag Reduction, Riblets, Navier–Stokes, DNS, Immersed Boundary, CPL

1. Introduction

Riblets are small, streamwise-aligned grooves that generate an anisotropic surface roughness, reducing turbulent friction drag below that of a smooth surface without the need for energy input. In their straight configuration, the section is shaped as triangles, blades, or parabolic profiles, with a sharp tip at the edge.
Riblets were first observed in nature on shark skin [3] and have since been studied for industrial purposes.
The ability of riblets to reduce skin friction is dependent on their size. The underlying physical mechanism for this effect was first described by Luchini et al. [20] and can be attributed to an offset between the virtual origins of the streamwise and spanwise velocity profiles, also known as longitudinal and perpendicular protrusion heights, respectively. The magnitude of drag reduction increases with the difference between the longitudinal and perpendicular protrusion heights. When the perpendicular protrusion height is smaller than the longitudinal one, the quasi-streamwise vortices associated with cross-flow move further away from the wall, thereby reducing the contribution of the wall cycle to turbulent kinetic energy production.

1.1. State of the art: straight riblets

Straight riblets have been extensively investigated through physical experiments [5, 27, 28] and Direct Numerical Simulations [8, 10, 11]. The drag-reducing regime in riblets can be classified into two categories: the viscous regime and the maximum drag-reduction regime. In the viscous regime, for very small riblets, the drag-reduction increases linearly with the size of the riblets, and the protrusion heights are sufficient to quantify the virtual origins associated with both mean and turbulent flows. On the other hand, the maximum drag reduction regime is characterized by the breakdown of the linear relationship due to the emergence of Kelvin-Helmholtz-like instabilities or the fall of the turbulent structures between the riblet tips, depending on the cross-section shape of the riblets [9, 11]. To accurately determine the origin of turbulence in this regime, it is necessary to take into account the slip length for the wall normal velocity as well [15].
For larger riblets, the drag-increasing phenomena become predominant, leading to an increase in friction drag above that of a smooth surface, finally reaching a fully rough behavior. This behavior is explained by the rise of larger scale structures such as the secondary motions [14]. Gatti et al. [12] found that riblets exhibit this behavior for only a limited range of sizes, after which the drag curve deviates from the expected fully rough asymptote. According to Garcia-Mayoral and Jimenez [11], the square root of the groove cross-section area l_g is the best parameter to characterize riblet size. Since our focus is on drag-reducing riblets with 60-degree tip angles, we use Bechert et al. [5]'s experimental data as a reference for straight riblets. This data suggests that for straight 60-degree tip angles, the expected maximum drag reduction is around 5% for l_g^+ between 10 and 11. It is generally assessed that, for any groove cross-section shape, the maximum drag reduction is usually achieved at $l_g^+ \approx 10.7 \pm 1$.
Riblets' impact has also been investigated through lower fidelity simulations, such as RANS and LES, that introduce some modelling hypothesis to the Navier-Stokes equations, so they can be solved with substantially lower computational effort, allowing studies at higher Reynolds number. Also in this context riblets have been proven to enhance the surface performance in terms of friction drag and efficiency. Some examples of RANS simulations are [6, 21], who both implemented peculiar boundary conditions to the $k-\omega$ SST turbulence model to account for the riblets presence. These simulations point out an enhancement of the aircraft behavior in both friction drag and efficiency, though it is difficult to extrapolate universal results in presence of very diverse geometries and flow configurations.

1.2. State of the art: sinusoidal riblets

The concept of sinusoidal riblets involves varying the spanwise position of the edge sinusoidally along the x-direction. This idea is inspired by the desire to combine the virtual origins effect, typical of straight riblets, with the effects of active spanwise forcing control [24]. This approach is expected to increase the viscous slope or extend the viscous regime to higher l_g^+, resulting in an increase in the maximum drag reduction provided by riblets. It is important to note, however, that the gains obtained from spanwise forcing control effects are expected to be much smaller than the typical $20-30\%$ viscous drag reduction achieved through active spanwise forcing, as the modification w.r.t. straight riblets is only a change in shape that preserves the passive nature of flow control.
The exercise of varying the spanwise position of the tips has already been conducted experimentally by [4, 26] and numerically by [25], but with different intent. In fact, the geometries investigated in these research studies do not induce the typical spanwise motions of spanwise forcing control. In contrast, studies such as [7] and [22] investigated sinusoidal riblets as a means to reproduce oscillating wall effects in experiments and LES simulations, respectively, but arrived at conflicting conclusions.

1.3. The challenge of simulating ribbed channels

All the DNS studies mentioned earlier have faced difficulties in simulating ribbed channel flows due to the presence of sharp edges. To resolve the flow around these geometric singularities, a large number of grid points is required, but computational resources are limited. As a result, previous researchers have had to make compromises to control computational cost.
Choi et al. [8] conducted simulations in channels with riblets on only one wall, using the opposite wall as a reference for measuring friction. However, this created an asymmetric flow, with different friction velocities on either side, leading to different friction Reynolds numbers. It is also unclear which value should be used for the free-stream velocity in calculating the friction coefficient. On the other hand, Garcia-Mayoral and Jimenez [11] only simulated riblets with a rectangular cross-section, enabling the collocation of the Cartesian grid points on the surface of the geometry. DNSs by Sasamori et al. [25] and Endrikat et al. [10] were performed in a minimal-span channel and therefore faced limitations due to the small domain size, making it difficult to

accurately evaluate the friction coefficient due to unphysical statistics far from the wall.
When simulating sinusoidal riblets, an additional requirement arises due to the periodic nature of boundary conditions, mandating the simulation of at least one full wavelength of the geometry.

1.4. Outline

After gaining preliminary insight into the numerical characteristics of the code used in Section 2, an innovative immersed boundary method that can describe complex geometries without the need for super-fine meshes at the edges is described in Section 3. The focus is on implementing the corner correction that imposes steady Stokes and Laplace solutions near geometrical singularities, such as the sharp edges of riblets. The improvement in code performance due to the corner correction is demonstrated in Section 4.1, where the protrusion heights for straight riblet geometry are evaluated and compared to the values obtained with sinusoidal riblets. In Sections 4.2 and 4.3, we present the results of turbulent Direct Numerical Simulations (DNS) of channel flows with straight and sinusoidal riblets, comparing the former to the results from Bechert et al. [5] and Endrikat et al. [10] for the same tip angle. In Section 4.4, we present observations about the position and intensity of the Quasi-Streamwise-Vortices with the λ_{CI} method for the straight geometry.
Throughout this thesis, we use x, y, and z to refer to the streamwise, spanwise, and wall-normal directions, respectively, with corresponding velocity components u, v, and w.

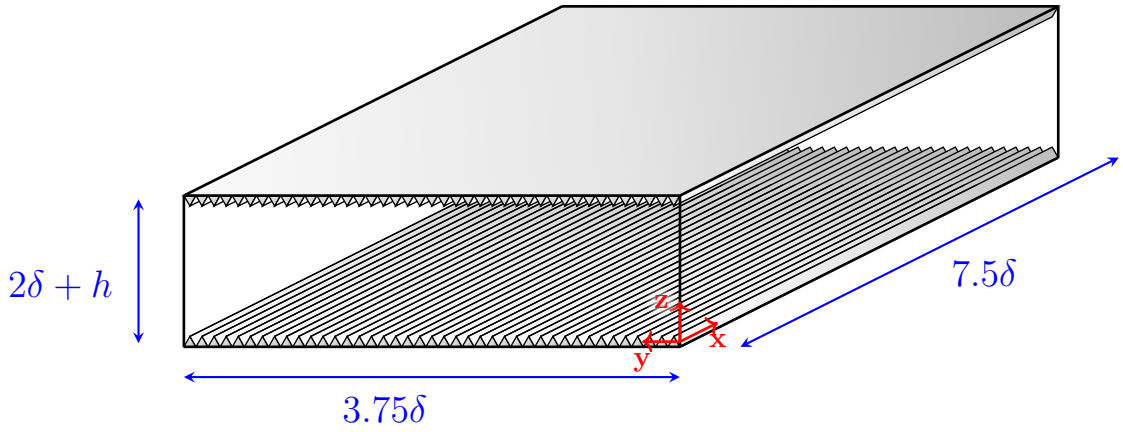

Figure 1: A visual representation of the computational domain. δ represents the semi-channel height.

2. Numerical method

DNS of fully developed turbulent channel flows are conducted at a friction Reynolds number $Re_\tau = 200$, defined as $Re_\tau = \frac{\delta u_\tau}{\nu}$. Here δ is the half-channel height, u_τ is the friction velocity, calculated as $u_\tau = (\tau_w/\rho)^{0.5}$, and ν is the kinematic viscosity. τ_w is the wall shear stress and ρ is the fluid density.
The DNS code, written in CPL [19] and introduced by Luchini [18], solves the incompressible Navier–Stokes equations written in primitive variables on a staggered Cartesian grid. Second-order finite differences are used in every direction. The momentum equations are advanced in time by a fractional time stepping method using a third-order Runge–Kutta scheme. The Poisson equation for the pressure is solved by an iterative successive over-relaxation (known as SOR) algorithm. The ribbed walls are dealt with via an implicit immersed-boundary method, and the equations are solved over a staggered cartesian grid. The grid is uniform in the stream- and spanwise direction; it is also uniform below the riblets tip in the wall-normal direction and it stretches with a geometrical series from the riblets tip to the half channel. Periodic boundary conditions are implemented in the streamwise and spanwise directions; no slip and no penetration boundary conditions are imposed at the wall. A sketch of the computational domain is shown in Figure 1. Note that the domain in the wall normal direction spans between the values $-h/2$ and $2\delta + h/2$, where h represents the riblets height. The zero coordinate lies at the riblets semi-height, allowing us to keep the same channel cross section as the smooth case; this is the correct set-up in order to compare the friction coefficient (C_f) between different geometries.
Turbulent simulations are performed with a Constant Pressure Gradient (CPG) [23] along the x-direction and at a constant CFL number equal to 1.2. The statistics are averaged for 400 time units, calculated as large-scale eddy turnover time $t\delta/u_\tau$. All geometries present triangular riblets with 60° tip angle and both walls are ribbed; the only variable geometrical parameter, apart form the values describing the sinusoidal evolution of the edge position, is the riblets size, defined by l_g^+; here and throughout the paper, the + superscript denotes quantities expressed in wall units. A summary of the geometrical parameters for domain and grid size can be found in

Table 1. Given the broad range of possible parameter values for defining the geometry of sinusoidal riblets, we select the values for the wavelength λ_x and the maximum angle β from [1], who studied a few configurations and identified two different interesting zones in the λ_x - β plane. We refer to these configurations as "LONG" and "SHORT", based on the wavelengths used. The selected parameters can be found in Table 2.

	l_g^+	Re_τ	L_x^+	L_y^+	δx^+	δy^+	δz^+
Grid 1	$0 \div 5.3$	200	1500	750	2.0	0.5	$0.8 \div 2.4$
Grid 2	$5.3 \div 17.1$	200	1500	750	2.0	1.0	$0.8 \div 2.4$

Table 1: Simulation parameters for the used grids: square root of the cross sectional area l_g^+, friction Reynolds number Re_τ, domain dimensions (L_x^+, L_y^+), grid spacing in streamwise (δx^+), spanwise (δy^+) and wall-normal (δz^+) directions.

Geometry	λ_x^+	β_{max}
STRAIGHT	∞	0°
LONG	1500	2°
SHORT	250	12°

Table 2: Geometric parameters determinating the shape of straight and sinusoidal riblets: wavelength (λ_x^+) and maximum inclination w.r.t. the x-axis (β_{max}).

3. Corner Correction

The implicit immersed-boundary method is continuous in terms of boundary crossing and numerically stable at all distances from the boundary [17, 18]. In this section we show how to integrate the corner correction with the immersed boundary conditions.
Here is how the temporal discretization of the momentum equations is performed for the i-th velocity component with the implicit immersed boundary formulation:

$$u_i^{n+1} = \frac{1}{1 + imbc\,\Delta t}\left[u_i^n + \Delta t\left(\frac{1}{Re}\nabla^2 u_i^n - \frac{\partial p^n}{\partial x_i} - (\mathbf{u}^n \cdot \nabla)u_i^n\right)\right]. \tag{1}$$

Here p is the pressure, Δt is the timestep, and the superscripts $n+1$, n denote the present and the previous timestep, respectevely.
In the general implicit immersed boundary framework the corrective term $imbc$ can be written as follows, with d_{k1}, d_{k2}, $k = x, y, z$ distances from the physical boundary in k-th direction, and d_{j1}, $d_{j2} = \delta k$ when there is no intersection with the boundary:

$$imbc = \frac{1}{\delta x^2}\frac{\delta x}{d_{x1}} + \frac{1}{\delta x^2}\frac{\delta x}{d_{x2}} + \frac{1}{\delta y^2}\frac{\delta y}{d_{y1}} + \frac{1}{\delta y^2}\frac{\delta y}{d_{y2}} + \frac{1}{\delta z^2}\frac{\delta z}{d_{z1}} + \frac{1}{\delta z^2}\frac{\delta z}{d_{z2}} - \frac{2}{\delta x^2} - \frac{2}{\delta y^2} - \frac{2}{\delta z^2}. \tag{2}$$

This term is identically zero when the stencil doesn't cross the boundary.
Near the physical boundaries the convective terms in the momentum equation contribute minimally to the solution, and can therefore be neglected. Additionally, since the time derivatives are of the same order as the convective terms, they too can be disregarded. As a result, we can assume that the solution near geometrical singularities is similar to the steady Laplace (for u) or Stokes (for v, w) solutions.
Based on this hypothesis, we can modify the immersed boundary terms to drive the solution locally toward the Laplace/Stokes solution (u^{lapl}, v^{st}, w^{st}) for a flow around a wedge.

3.1. Corner correction for the streamwise velocity component

Under the previously stated hypothesis, near geometrical singularities the streamwise velocity component satisfies the Laplace equation. Here the Laplace equation is discretized in an implicit immersed boundary framework

(everything is multiplied by $u^{n+1}(x)$):

$$\begin{aligned}&\left\{\frac{1}{\delta x^2}\frac{\delta x}{d_{x1}}\,u^{lapl}(x+d_{x1})+\frac{1}{\delta x^2}\frac{\delta x}{d_{x2}}\,u^{lapl}(x-d_{x2})+\frac{1}{\delta y^2}\frac{\delta y}{d_{y1}}\,u^{lapl}(y+d_{y1})+\right.\\&\left.+\frac{1}{\delta y^2}\frac{\delta y}{d_{y2}}\,u^{lapl}(y-d_{y2})+\frac{1}{\delta z^2}\frac{\delta z}{d_{z1}}\,u^{lapl}(z+d_{z1})+\frac{1}{\delta z^2}\frac{\delta z}{d_{z2}}\,u^{lapl}(z-d_{z2})\right\}\frac{u^{n+1}(x)}{u^{lapl}(x)}+\\&-\left[\frac{1}{\delta x^2}\frac{\delta x}{d_{x1}}+\frac{1}{\delta x^2}\frac{\delta x}{d_{x2}}+\frac{1}{\delta y^2}\frac{\delta y}{d_{y1}}+\frac{1}{\delta y^2}\frac{\delta y}{d_{y2}}+\frac{1}{\delta z^2}\frac{\delta z}{d_{z1}}+\frac{1}{\delta z^2}\frac{\delta z}{d_{z2}}\right]u^{n+1}(x)=0\,.\end{aligned}\tag{3}$$

It is possible to susbtitute this discretized Laplace equation into Equation (1) to get the momentum equation for u accounting for the corner correction.

$$\begin{aligned}&\left\{1+\Delta t\,\frac{\nu}{u^{lapl}(x)}\left[\frac{1}{\delta x^2}\frac{\delta x}{d_{x1}}\,u^{lapl}(x+d_{x1})+\frac{1}{\delta x^2}\frac{\delta x}{d_{x2}}\,(x-d_{x2})+\right.\right.\\&+\frac{1}{\delta y^2}\frac{\delta y}{d_{y1}}\,u^{lapl}(y+d_{y1})+\frac{1}{\delta y^2}\frac{\delta y}{d_{y2}}\,u^{lapl}(y-d_{y2})+\frac{1}{\delta z^2}\frac{\delta z}{d_{z1}}\,u^{lapl}(z+d_{z1})+\\&\left.\left.+\frac{1}{\delta z^2}\frac{\delta z}{d_{z2}}\,u^{lapl}(z-d_{z2})-\frac{2}{\delta x^2}-\frac{2}{\delta y^2}-\frac{2}{\delta z^2}\right]\right\}u^{n+1}(x)=u^n(x)+RHS(u^n(x))\end{aligned}\tag{4}$$

$u^{lapl}(x)$ is the solution to the Laplace equation at the point (x,y,z) for the wedge geometry as shown in Figure 2. The term multiplying Δt is the *imbc* term that takes into account the corner correction. The right-hand-side (RHS) term is treated explicitly and is comprehensive of the Laplacian, the pressure gradient and the convective terms.

3.2. Corner correction for the spanwise and wall-normal velocity components

Following the same reasoning we write the discretized Stokes equation for the spanwise velocity component in the implicit immersed boundary framework. The same holds for the wall-normal one:

$$\begin{aligned}&\left\{-\frac{1}{\mu}\left[p^{st}\left(y+\frac{\delta y}{2}\right)-p^{st}\left(y-\frac{\delta y}{2}\right)\right]\frac{1}{\delta y}+\frac{1}{\delta x^2}\frac{\delta x}{d_{x1}}\,v^{st}\,(x+d_{x1})+\frac{1}{\delta x^2}\frac{\delta x}{d_{x2}}\,v^{st}\,(x-d_{x2})+\right.\\&\left.+\frac{1}{\delta y^2}\frac{\delta y}{d_{y1}}\,v^{st}\,(y+d_{y1})+\frac{1}{\delta y^2}\frac{\delta y}{d_{y2}}\,v^{st}\,(y-d_{y2})+\frac{1}{\delta z^2}\frac{\delta z}{d_{z1}}\,v^{st}\,(z+d_{z1})+\frac{1}{\delta z^2}\frac{\delta z}{d_{z2}}\,v^{st}(z-d_{z2})\right\}\frac{v^{n+1}(x)}{v^{st}(x)}+\\&-\left[\frac{1}{\delta x^2}\frac{\delta x}{d_{x1}}+\frac{1}{\delta x^2}\frac{\delta x}{d_{x2}}+\frac{1}{\delta y^2}\frac{\delta y}{d_{y1}}+\frac{1}{\delta y^2}\frac{\delta y}{d_{y2}}+\frac{1}{\delta z^2}\frac{\delta z}{d_{z1}}+\frac{1}{\delta z^2}\frac{\delta z}{d_{z2}}\right]v^{n+1}(x)=0\,.\end{aligned}\tag{5}$$

By substituting this equation into Equation (1) we get the discretized momentum equations for the spanwise/wall-normal velocity components accounting for corner correction:

$$\begin{aligned}&\left\{1+\Delta t\,\frac{\nu}{v^{st}(x)}\left[-\frac{1}{\mu}\left(p^{st}\left(y+\frac{\delta y}{2}\right)-p^{st}\left(y-\frac{\delta y}{2}\right)\right)\frac{1}{\delta y}+\frac{1}{\delta x^2}\frac{\delta x}{d_{x1}}\,v^{st}(x+d_{x1})+\right.\right.\\&+\frac{1}{\delta x^2}\frac{\delta x}{d_{x2}}\,v^{st}(x-d_{x2})+\frac{1}{\delta y^2}\frac{\delta y}{d_{y1}}\,v^{st}(y+d_{y1})+\frac{1}{\delta y^2}\frac{\delta y}{d_{y2}}\,v^{st}(y-d_{y2})+\frac{1}{\delta z^2}\frac{\delta z}{d_{z1}}\,v^{st}(z+d_{z1})+\\&\left.\left.+\frac{1}{\delta z^2}\frac{\delta z}{d_{z2}}\,v^{st}(z-d_{z2})-\frac{2}{\delta x^2}-\frac{2}{\delta y^2}-\frac{2}{\delta z^2}\right]\right\}v^{n+1}(x)=v^n(x)+RHS(v^n(x))\,.\end{aligned}\tag{6}$$

v^{st}, w^{st}, p^{st} are the solutions to the Stokes problem. Their expressions can be easily derived in polar coordinates centered at the riblet tip as we can write the Stokes equation as a system for vorticity ω and stream function ψ:

$$\nabla^2\omega=0 \qquad\qquad \nabla^2\psi=-\omega\,.\tag{7}$$

The solutions for a wedge geometry $v^{st}(r,\theta)$, $w^{st}(r,\theta)$ are shown in Figure 2. The corner correction version of the implicit immersed boundary is only considered when points are near the geometrical singularity, specifically when the distance from the tip is lower than $2\delta_\nu$, where δ_ν is the viscous length. All the other points only feature the classical implicit immersed boundary implementation (2).

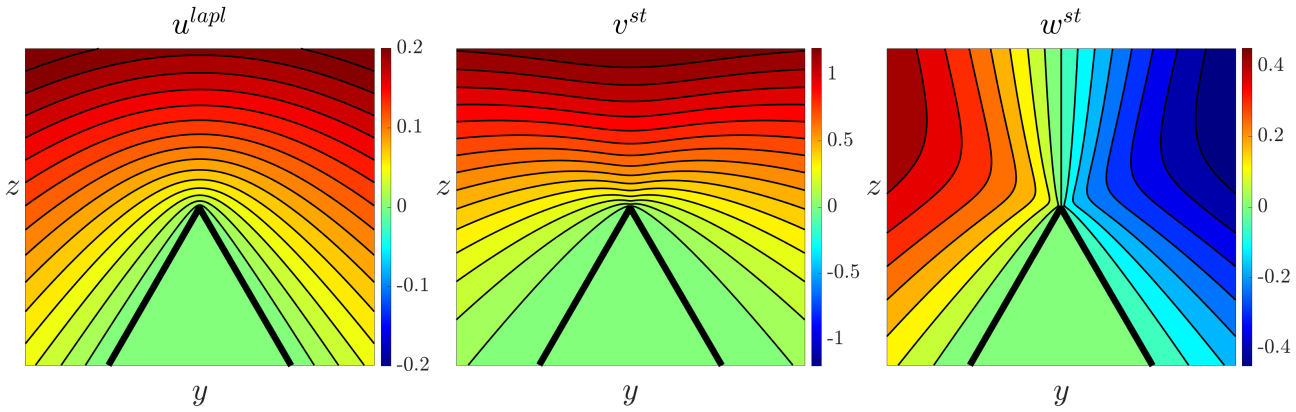

Figure 2: Solutions for the Laplace and Stokes problems. Visualizing p^{st} is problematic due to the singularity it has at the tip.

For sinusoidal riblets the situation complicates a little bit. Equation (4) and (6) can be rewritten from a defferred correction point of view:

$$\begin{aligned} u^{n+1} &= u^n(x) + RHS(u^n(x)) + d_u^{n+1}\,, \qquad with:\ d_u^{n+1} = corr_L\, u^{n+1}\,, \\ v^{n+1} &= v^n(x) + RHS(v^n(x)) + d_v^{n+1}\,, \qquad with:\ d_v^{n+1} = corr_S\, v^{n+1}\,. \end{aligned} \tag{8}$$

Being $corr_L$, $corr_S$ the immersed boundary coefficients modified with the corner corrections coming from the Laplace and Stokes solutions. This implementation is only valid for the velocity components aligned and perpendicular to the edge, referred to as $(\widetilde{u},\, \widetilde{v})$ in Figure 3. For velocities in the main reference system, the deferred corrections result in a non-diagonal 2x2 matrix, as shown in equation (9). The appearance of v^{n+1} in the momentum equation for u would hinder the costless implicit discretization and make the system unsolvable with a staggered grid, having to deal with more variables than equations.

$$\begin{bmatrix} d_u \\ d_v \end{bmatrix} = \begin{bmatrix} corr_L\, \cos^2\beta + corr_S\, \sin^2\beta & (corr_L - corr_S)\sin(2\beta)/2 \\ (corr_S - corr_L)\sin(2\beta)/2 & corr_S\, \cos^2\beta + corr_L\, \sin^2\beta \end{bmatrix} \begin{bmatrix} u^{n+1} \\ v^{n+1} \end{bmatrix} \tag{9}$$

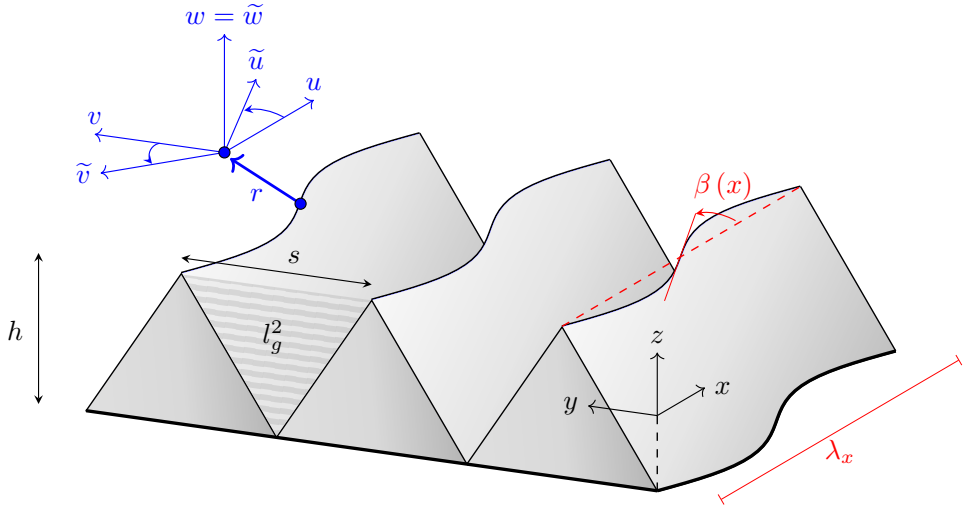

Figure 3: Geometrical parameters describing the riblets: h is the riblet height, s is the spacing, λ_x^+ is the wavelength, β the local angle between the riblet crest and the x-axis. $\widetilde{u}$, $\widetilde{v}$ are the velocity components aligned with the riblet edge, rotated by $\beta(x)$ w.r.t. the velocity components in the main reference frame $(u,\, v)$.

For this reason, we choose to treat the extra-diagonal terms explicitly, which restores the advantages of the costless implicit formulation and makes the equations solvable with a staggered grid. To tackle the staggered grid problem, we interpolate the v velocity component on the u-grid, while maintaining continuity with boundary crossings. The same reasoning applies to the momentum equation for v. In this way, we can sum the extra-diagonal terms to the right-hand-side term, which becomes $RHS\,(u^n(x),\, v^n(x))$. The corner-corrected immersed boundary coefficients take into account both $corr_L$ and $corr_S$ as seen in Equation (9). We conducted an analysis of the impact of extra-diagonal terms on the calculation of protrusion heights in laminar simulations, comparing the results to the ones obtained by completely disreguarding the extra-diagonal terms, whose contribute scales with β_{max}. Their impact decreases with the decrease of β_{max} and has been found to be on the order of 1% for riblets with $\beta_{max} = 30°$.

4. Results

In this section, we present the results of both laminar and turbulent simulations. In both types of simulation, the significant impact of the corner correction implementation near geometrical singularities is assessed, particularly in the evaluation of drag reduction by riblets. For laminar simulations we compute the protrusion heights for straight riblets, and compare them with the expected values, that can be calculated analitically like in Luchini et al. [20]; protrusion heights for sinusoidal riblets are calculated as well, to understand the impact on the laminar solution. However, the analytical solution is not available for comparison. Turbulent results will be presented in terms of friction coefficient C_f and shift in the mean velocity profile ΔU^+. A comparison with the experimental results from Bechert et al. [5] and DNS results from Endrikat et al. [10] for the same tip angle will be conducted, as well as a comparison between straight and sinusoidal riblets. A short sections studying the position and intensity of the Quasi-Streamwise-Vortices for varying l_g^+ in the straight riblets configuration concludes the results.

4.1. Protrusion Heights

The concept of protrusion heights was first introduced by Luchini [20] in the context of grooved surfaces. A protrusion height is a lenght that defines a virtual smooth wall below the riblets tip that would yield the same spanwise-averaged velocity profile as the one obtained with a grooved wall (Figure 4). This is why they are also referred to as virtual origins. The concept applies to both longitudinal and cross flows, defining two different lengths: longitudinal and transverse protrusion heights ($h_\parallel$, $h_\perp$). We will also refer to them as (l_X, l_Y). The protrusion heights are usually normalized with the period of corrugations, making them a purely geometrical parameter that depends only on the grooves' section shape.

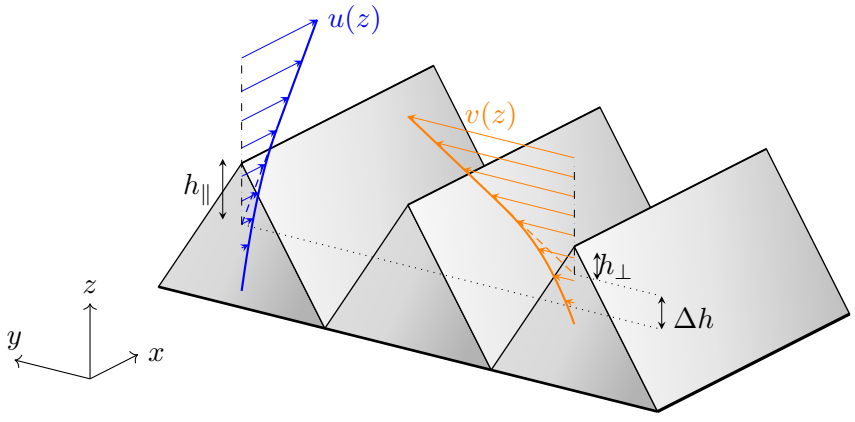

Figure 4: A visual representation of the difference between the protrusion heights, Δh. The blue (orange) velocity profile represents the mean stream-wise (span-wise) laminar flow over the ribbed wall.

This concept is crucial for understanding ribbed surfaces behavior because the difference between the two values $\Delta h = h_\parallel - h_\perp$ provides a clear indication of how much the ribbed wall impedes cross-flow relative to longitudinal flow. If the virtual origin for transverse flow lies above that of the mean flow, it means that the cross flow will perceive a smaller channel height. This has great importance for turbulent flows as well, as the cross flow can be

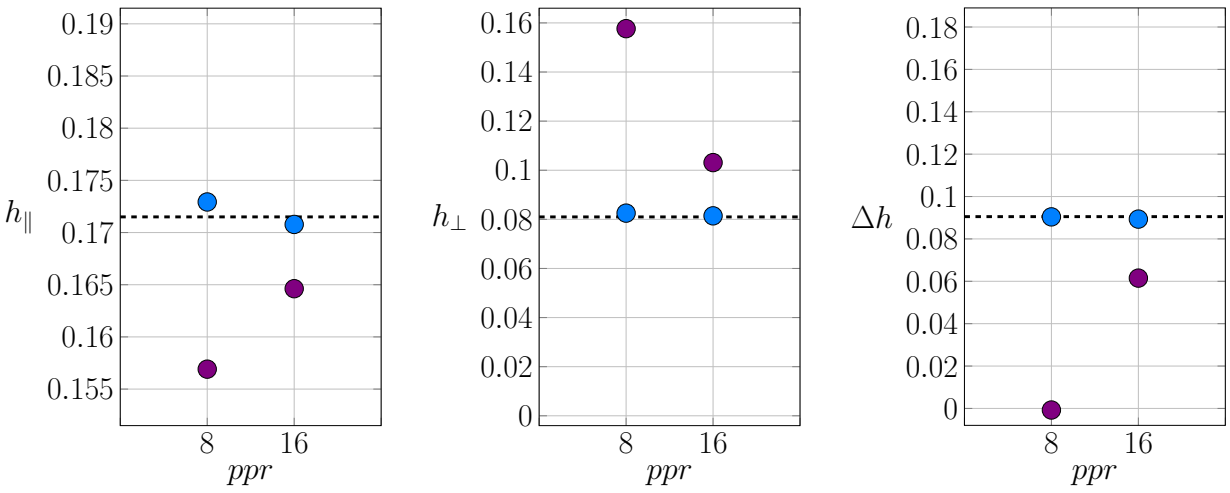

Figure 5: Protrusion heights values compared to the analytical results from Luchini [20] for straight riblets. Azure points: corner correction activated. Violet points: corner correction deactivated. "ppr" indicates the number of points per riblet along the spanwise direction.

associated to turbulence, since many turbulent structures present velocity components in the spanwise direction. In this context, the turbulent flow, perceiving a lower channel height than that associated to the mean flow, experiences a higher viscous dissipation resulting in a reduced turbulent kinetic energy near the wall.
Protrusion height values can be calculated numerically with high accuracy for any groove section [20], and these reference values are represented with dashed lines in Figure 5. Our aim is to calculate these values using our code with a moderate number of points. We select two grids with respectevely 8 and 16 points per riblet (ppr) in the spanwise direction. These grid resolution correspond to the grids "Grid 1" and "Grid 2" described in Table 1 for a geometry with $l_g^+ = 5.3$. The wall-normal resolution is the same as that used in one of the turbulent simulations at $Re_\tau = 200$, implying the use of approximately 17 points per riblet height. We impose unitary shear in the streamwise and spanwise directions. The results for straight riblets are shown in Figure 5. As we can observe, the corner correction is of primary importance for accurately predicting the protrusion heights values. Notably, without the corner correction, the grid with 8 points per riblet is not even capable of predicting the correct sign of Δh. When the corner correction is activated, on the other hand, the code can predict the protrusion heights values with very good accuracy in both cases.
As a result, the immersed boundary implementation that takes into account a corner correction near geometrical singularities can be used in turbulent simulations to introduce the virtual origin contribution given by riblets, but without the need of using a much finer resolution than the one required for a turbulent smooth channel.
Protrusion heights can be defined for sinusoidal riblets in the same way as for straight riblets. However, there is a difference in that the streamwise direction loses homogeneity with sinusoidal riblets, requiring at least one full wavelength for laminar simulations. Although the tip angle remains the same as for the straight geometry, variations in the values of protrusion heights are expected due to the differing effects of sinusoidal riblets on impeding longitudinal and cross flow compared to straight riblets. The results for both 8 and 16 points per riblet are presented in Figure 6.

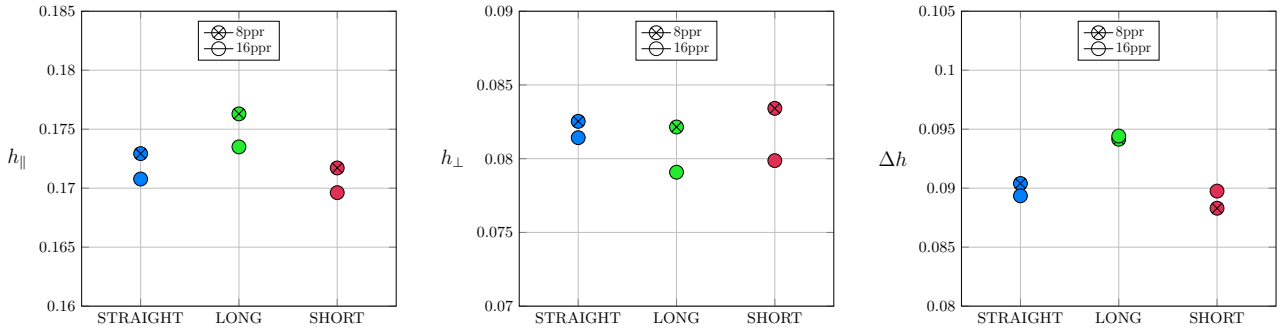

Figure 6: Protrusion heights values for the considered geometries.

The main takeaways from Figure 6 are that the LONG geometry impedes longitudinal flow the least, followed by the STRAIGHT and the SHORT ones, while for the perpendicular one the trend is reversed. Consequently, the LONG geometry has the highest Δh, while the STRAIGHT and SHORT geometries yield similar values. The difference between the two resolutions (8 and 16 ppr) introduces a shift for both protrusion heights; this shift is cancelled out when calculating Δh, as the differences between the two resolutions are much smaller.
When considering turbulent simulations, the virtual origins affecting friction drag are the mean flow and the turbulent virtual origins, namely l_U and l_T. In the viscous regime, where $h_\parallel = l_X = l_U$ and $h_\perp = l_Y = l_T$, and ΔU^+ is proportional to Δh, we expect the LONG geometry to have a higher viscous slope than the other two configurations. These predictions will be verified in Section 4.2.

4.2. Turbulent Simulations: Friction Coefficient

Even though the protrusion heights values obtained from very inexpensive laminar simulations give a clear indication about the effectiveness of a grooved surface in reducing the turbulent skin friction, they are not enough to correctly assess the amount of drag reduction in a turbulent ribbed channel flow, and they don't provide indication about the optimal groove cross-section area $l_{g,opt}$. The only information they provide is about the slope of the viscous region. As explained by Ibrahim et al. [15] in the context of virtual origin and slip lengths, when riblets are large enough setting virtual origins for the longitudinal and transverse flow is not enough to correctly predict the right behavior of a turbulent flow. This means that the protrusion heights are not enough to assess the amount of drag reduction provided by the surface as a virtual origin for the wall-normal velocity should also be considered to predict the correct virtual origin for turbulence. A more detailed discussion will follow in Section 4.3. This breakdown of the viscous regime, as explained by Garcia-Mayoral and Jimenez [11], is due to the rise of Kelvin-Helmholtz-like instabilities and secondary motions between the riblets tips.
The easiest way to quantify drag reduction in a channel flow driven by a Constant Pressure Gradient is to compare the friction coefficient with that of a smooth channel at the same Re_τ and with the same cross-section area. The C_f is computed as $C_f = 2/(U_b^+)^2$, where U_b is the bulk velocity. In Figure 7 we plot the values of $\Delta C_f\%$ for different values of l_g^+ for the straight riblets configuration. ΔC_f is defined as the ratio between $C_f - C_{f,0}$ and $C_{f,0}$, with $C_{f,0}$ being the friction coefficient of a reference smooth channel, and C_f the friction coefficient of the controlled channel. The plus-coordinates are adimensionalized taking into account the value of the wall shear stress τ_w at the origin for turbulence $l_T = h/2 - z_T$; the procedure on how to calculate it will be shown in Section 4.3.

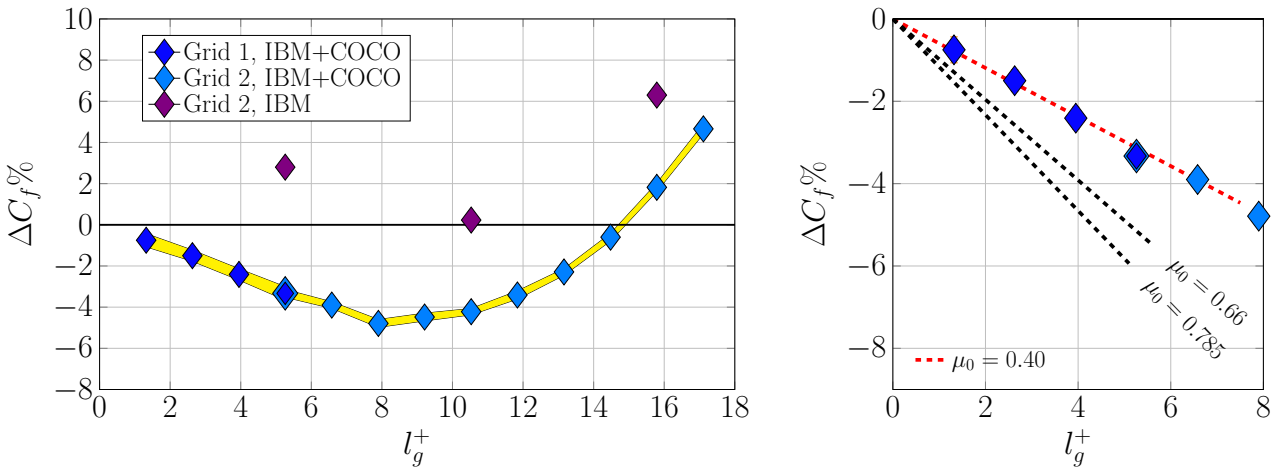

Figure 7: Drag Reduction curve for STRAIGHT riblets. Grid 1 and Grid 2 are described in Table 1. IBM refers to the classic implicit immersed boundary implementation, COCO refers to the corner correction activated at geometrical singularities. The yellow area represents the temporal uncertainty. On the right we focus on the slope of the viscous regime and μ_0 is representative of linear coefficient between the riblet size and drag reduction.

The first point to be made is that the corner correction has once again a great impact on the results. The geometries simulated without corner correction are never able to predict drag reduction. When corner correction is activated small riblets provide, as expected, a linear increase of drag reduction, and at $l_g^+ \approx 8$ the breakdown of the viscous region is visible. From the values of ΔC_f it is possible to extrapolate the slope of the linear region

$\mu_0 \approx 0.40$ compared to predictions from Bechert et al. [5] ($\mu_0 = 0.785$), Jimenez [16] ($\mu_0 = 0.66$). These values for μ_0 are not very relevant when looking at ΔC_f, being this parameter Reynolds dependent. The geometry with $l_g^+ \approx 5.3$ has been simulated with two different spatial resolutions, respectively with $\delta y^+ = 1$, $\delta y^+ = 0.5$ (8 ppr, 16 ppr), and they both give the exact same result, similarly to the laminar simulations (Figure 5).

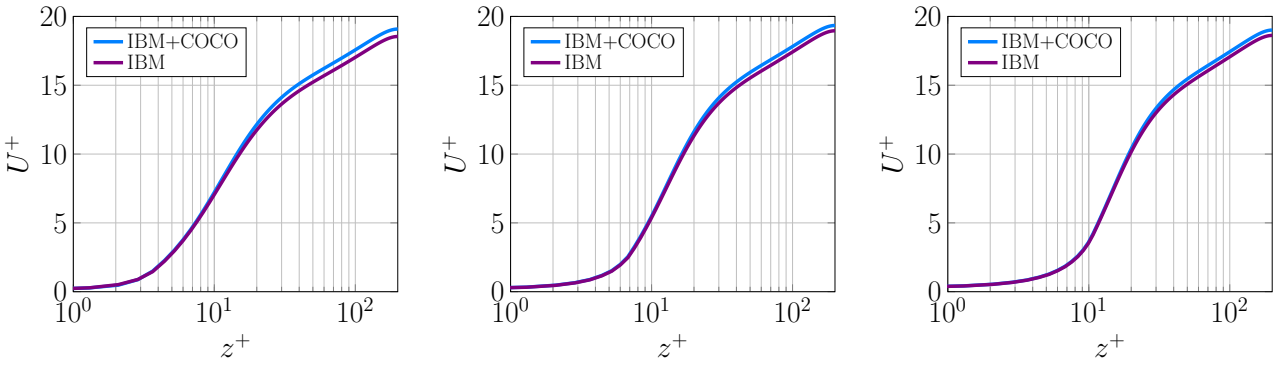

Figure 8: Comparisons of the mean velocity profiles with and without corner correction for respectevely $l_g^+ \simeq 5.2, 10.4, 15.5$. The profiles labelled as "IBM+COCO" take into account the corner correction, the others don't.

An assessment of the impact of the corner correction can also be obtained by looking at the mean velocity profiles for the same riblets size with corner correction activated and deactivated (Figure 8). It is possible to observe how, even though the correction is applied only at the close proximity of the edges, its effect is visible far from the boundary, as a shift in the velocity profile. Basically, when using the correction, we are imposing the slip lengths to a plane channel wall, similarly to what was done by Ibrahim et al. [15].

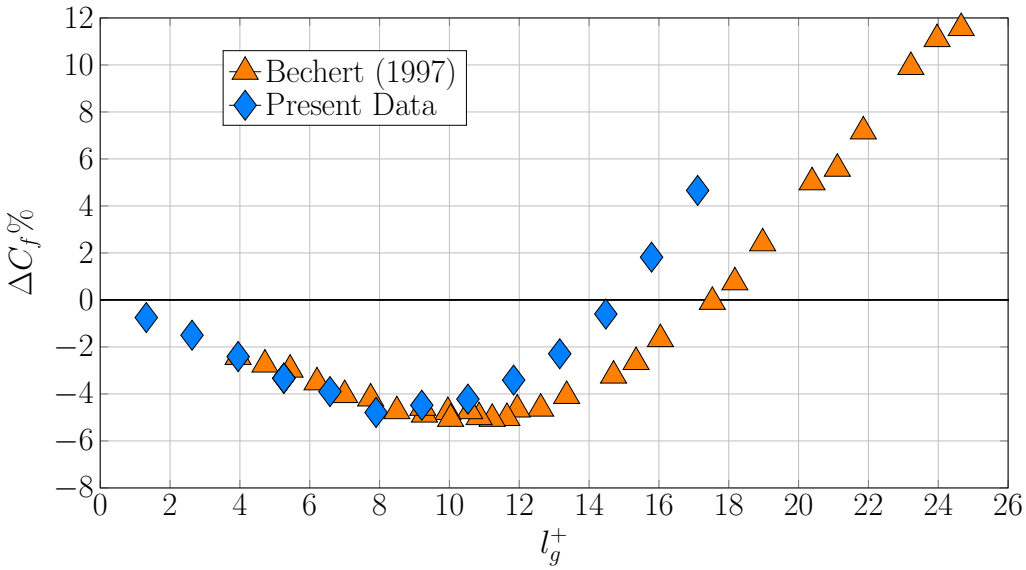

Figure 9: Straight riblets ΔC_f values for different l_g^+ compared to data from Bechert et al.[5]. The $+$ adimensionalization takes into account a unitary u_τ, differently from what we do in Section 4.3.

In Figure 9 our results for straight riblets are compared to the results from Bechert et al. [5] for the same tip angle. It is important to note that ΔC_f is not a Re_τ independent parameter [13], and Bechert[5], who conducted experiments with the Constant Flow Rate (CFR) configuration, varied Re_τ while changing l_g^+. However, their Reynolds numbers are similar to ours, and the dependence of ΔC_f on Reynolds is moderate. For these reasons, we observe good agreement between the two datasets, especially regarding the slope of the viscous regime and the value of the maximum drag reduction. As we increase the riblets size, we notice that the two datasets diverge, with zero-drag-reduction occurring at $l_{g,0}^+ \approx 15$, compared to their $l_{g,0}^+ \approx 17.5$, and a different position

of the peak. We explain this behavior by pointing out that as we increase l_g^+, we are physically increasing the size of the riblets compared to the channel height, since we keep a constant $Re_\tau = 200$. For larger riblets, the riblet height is approximately 10% of the channel semi-height. Consequently, it is no longer possible to consider the ribbed wall as a type of roughness, and the ΔC_f values are affected. One way to avoid this phenomenon would be to increase the Reynolds number.
The behavior of sinusoidal riblets varying their size can be investigated in the same fashion. Dag reduction curves in terms of $\Delta C_f\%$ for the LONG and SHORT geometries are displayed in Figure 10. The grid and domain characteristics are the same as those described in Table 1.

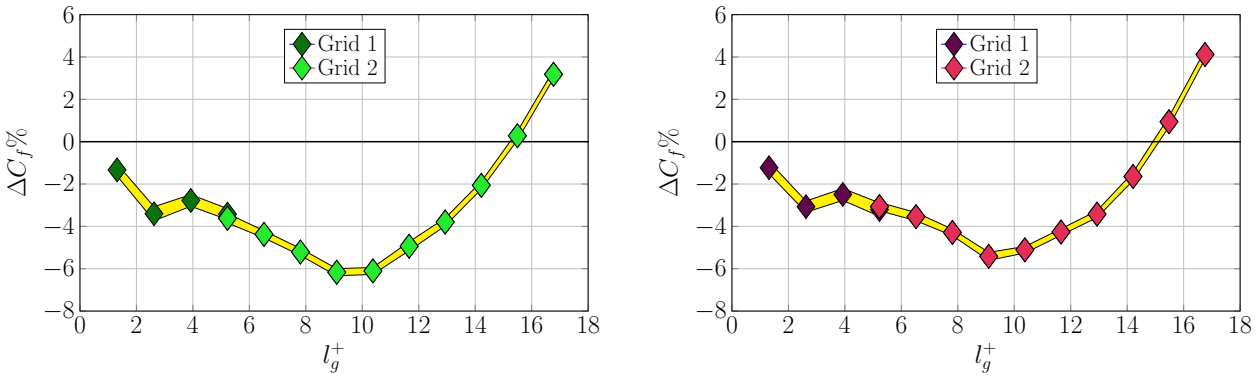

(a) LONG (b) SHORT

Figure 10: Drag Reduction curves for sinusoidal riblets. The yellow area represents the temporal uncertainty.

It is possible to observe that, in this case as well, the point at $l_g^+ \approx 5$ exhibits good grid independence of the results. The peak is located at around $l_g^+ = 10$, and its value exceeds 6% for the LONG geometry. For small riblets, some inaccuracies are visible, especially the point at $l_g^+ \approx 2.5$, which does not fit well with the linear law that is expected in the viscous region. We will discuss possible reasons for this behavior in Section 5.
In Figure 11, the difference between the drag reduction curves of straight and sinusoidal riblets is displayed. The latter yield higher drag reduction in both cases, with the LONG geometry outperforming the SHORT one by around 0.5%. The drag reduction achieved by straight riblets is enhanced by 13% with the SHORT configuration and by 29% with the LONG configuration.

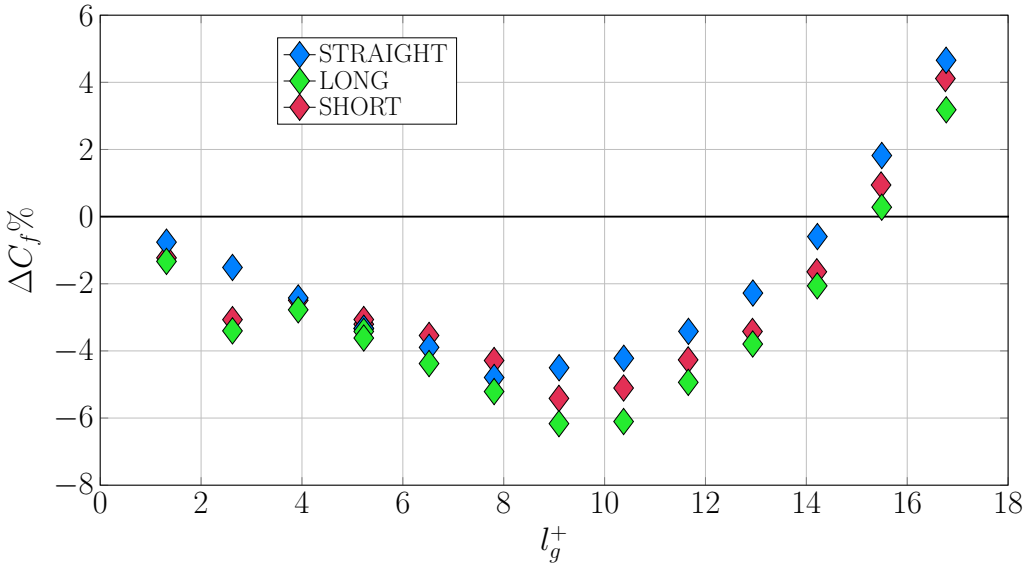

Figure 11: Drag reduction curves for all geometries.

It is also noticeable that despite the low Reynolds number of our simulations, which should negatively impact the drag reduction at the largest l_g^+, the peak of the drag reduction curves occurs at a larger riblet size when compared to the straight configuration. The LONG geometry, in particular, seems to be able to extend the viscous region to higher l_g^+ than the classic straight configuration. Furthermore, when compared to the other

geometries, the LONG geometry features a higher linear slope, in accordance with the predictions for the viscous region from our results in Section 4.1. As a result of the expansion of the viscous regime, the drag reduction curve intersects the zero-drag-reduction axis at higher l_g^+ when compared to straight riblets.

4.3. Turbulent Simulations: ΔU^+

ΔU^+ is a Re_τ-independent parameter used to evaluate drag reduction [13]. It represents a shift in the mean velocity profile, with an upward shift indicating drag reduction due to riblets. Assuming that the presence of flow control, in this case riblets, only causes a shift in the mean velocity profile without affecting the parameters of the logarithmic law such as the von Karman constant (k) and the near-wall intercept (B_1), and denoting the values related to the smooth reference channel with the subscript $_0$, we can write the friction law as follows:

$$\sqrt{\frac{2}{C_f}} - \sqrt{\frac{2}{C_{f,0}}} = \frac{1}{k} ln \frac{Re_\tau}{Re_{\tau,0}} + \Delta B \,. \tag{10}$$

This can be used to predict the shift ΔB^+ of the mean velocity profiles. In fact, if we consider a constant flow rate setup such as Bechert's, and we substitute the constraints of constant flow rate (CFR), $C_f = C_{f,0}(1-DR)$ and $Re_\tau = Re_{\tau,0}\sqrt{1-DR}$, we can solve for ΔB as follows: [13]

$$\Delta B^+ = \sqrt{\frac{2}{C_{f,0}}} \left[(1-DR)^{-0.5} - 1\right] - \frac{1}{2k} ln(1-DR) \,. \tag{11}$$

The parameter DR represents the drag reduction calculated as the ratio between $\Delta C_f = C_{f,0} - C_f$ and $C_{f,0}$. In this way, we can obtain ΔB^+ values corresponding to the ΔC_f data from Bechert et al.[5] without the need to analyze their velocity profiles, which are unknown. We slightly correct these values, as Equation (11) accounts for a logarithmic velocity profile without considering that the finite size of riblets modifies the shape of the velocity profile close to the wall. From our results, we select geometries with a similar h/δ ratio to those from Bechert et al. [5] and calculate the difference in flow rate between these profiles and the reference smooth profile, which would be zero for riblets of vanishing height (or at very large Re_τ). We then redistribute this flow rate in the remaining portion of the channel and obtain a shift in the velocity profile that must be added to ΔB^+ from Equation (11). With this procedure, we can compare these results with ΔU^+ values from our velocity profiles and from Endrikat et el. [10].

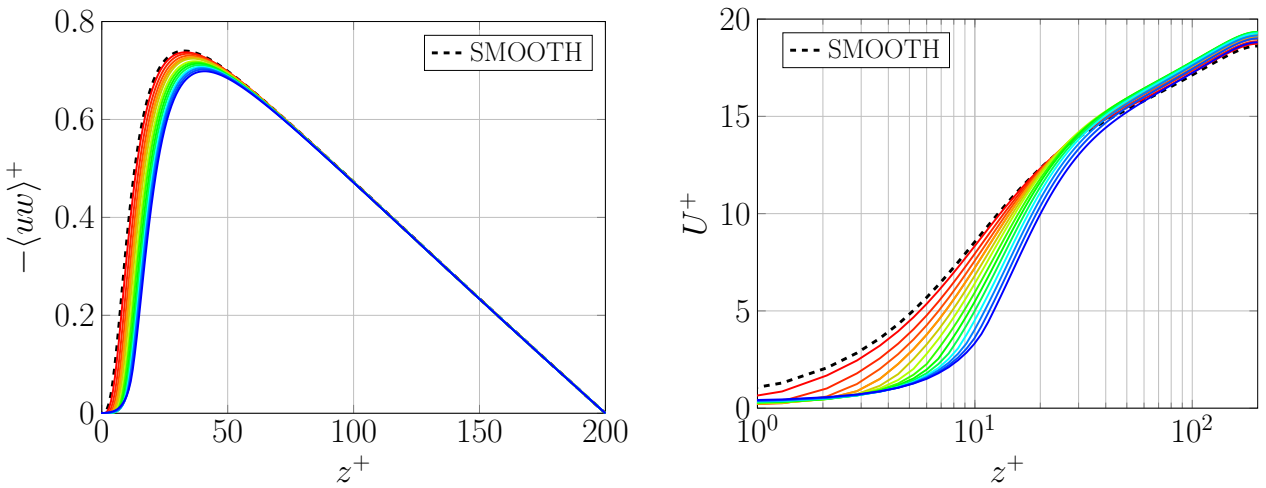

Figure 12: Plots of $\langle uw \rangle^+$, U^+ for straight riblets.

The next step is to calculate ΔU^+ for our simulations using the mean velocity and turbulent shear stress profiles, as explained by Ibrahim et al. [15]. The procedure consists of shifting the mean velocity profile by a quantity that we call z_T^+ and evaluating the difference between the considered U^+ profile and that of a smooth channel. The wall-normal shift z_T^+ is the same as the one applied to the turbulent shear stress profile $\langle uw \rangle^+$ of the ribbed channel so that it can match the profile of a smooth channel. At this point, the mean velocity profiles share the same virtual origin for turbulence. After correctly adimensionalizing the profiles in plus coordinates that take into account the "true" τ_w measured at the origin of turbulence, we should be able to see a rigid vertical

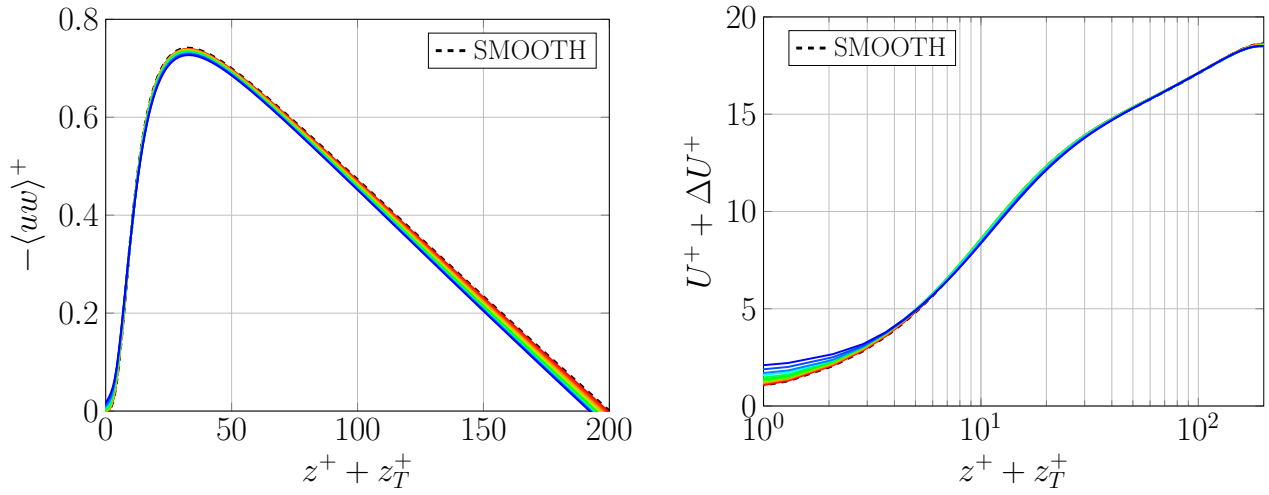

Figure 13: Plots of $\langle uw\rangle^+$, U^+ for straight riblets after a wall normal shift of z_T^+, rescaling with the correct plus-coordinates, and a vertical translation of ΔU^+.

displacement between the mean velocity profiles of the smooth and ribbed channels. This displacement is labeled as ΔU^+, with $-\Delta U^+ = l_U^+ - l_T^+$, where l_U^+ is the virtual origin for the mean velocity and l_T^+ is the virtual origin for turbulence. The profiles U and $\langle uw\rangle$ represent the u and uw fields mediated along the homogeneous directions and through time.

In the original formulation proposed by Ibrahim et al.[15], the wall of the smooth channel is positioned at the riblet tips ($z = 0$). As a result, the shift that is applied to align the $\langle uw\rangle^+$ profiles is equivalent to the virtual origin for turbulence, denoted as l_T^+. In our case, however, the smooth wall is situated at half the height of the riblets, in order to maintain an equivalent channel cross-sectional area. Consequently, the shift z_T that we derive from overlapping the $\langle uw\rangle^+$ profiles differs from the virtual origin for turbulence l_T^+, which should be measured from the riblet tips. To resolve this discrepancy, we define l_T as $l_T = h/2 - z_T$, to represent the virtual origin for turbulence.

In Figure 12, we present the mean velocity and turbulent shear stress profiles for the STRAIGHT geometry. The $\langle uw\rangle^+$ profiles clearly indicate that riblets induce a wall-normal shift in the turbulent shear stress. After the appropriate shift and adimensionalization, we observe that the $\langle uw\rangle^+$ profiles become highly similar. For consistency the same wall normal shift is applied to the mean velocity profile, and overlap the selected profiles with the reference profile of the smooth channel to obtain some overlapping over the logarithmic region, with the quantity summed being ΔU^+. Although there are some minor variations in the profiles due to the physical presence of riblets of varying sizes in the near-wall region, it is possible to observe that the profiles overlap almost perfectly across their entire span.

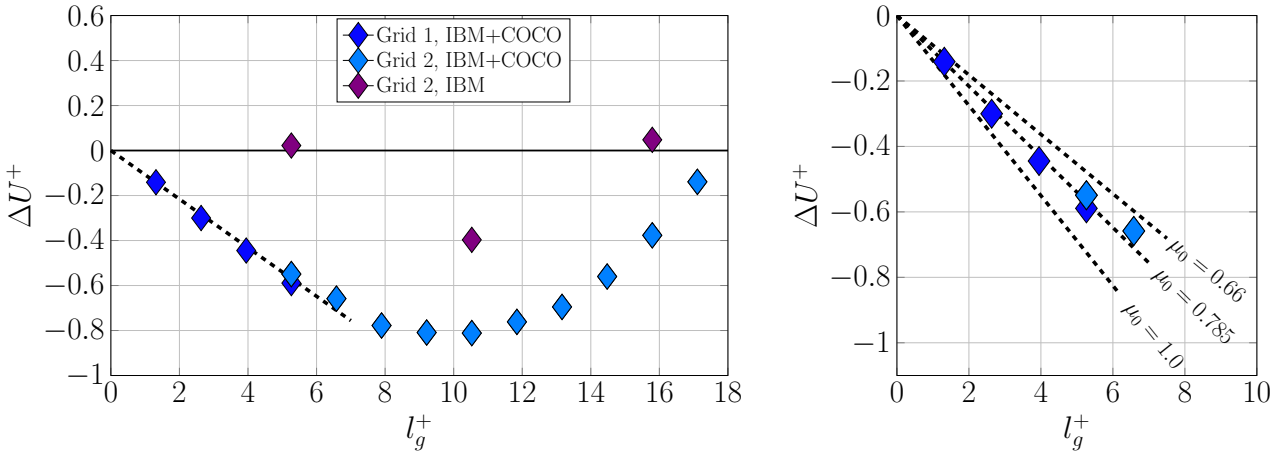

Figure 14: ΔU^+ values obtained for different l_g^+ for straight riblets. On the right we focus on the slope of the viscous regime. The $+$ adimensionalization is done considering the value of τ at the origin of turbulence $z = h/2 - l_T$ as τ_w.

In Figure 14 the values of ΔU^+ for straight riblets w.r.t. the riblets size l_g^+ are plotted. The values of ΔU^+ are adjusted in a similar way as we did for ΔU^+ values calculated from [5], to account for the loss of flow rate near the wall due to the low Reynolds number, that, for the bigger values of l_g^+, forces us to have riblets that are too big w.r.t. the channel height. Similarly to the ΔC_f plot (Figure 7), we can see how the geometries simulated without corner correction yield very different results from the expected ones, with only one out of three able to predict drag reduction. As regards the geometry simulated with the two grids, the results are in accordance, though slightly different. When looking at the viscous regime we can once again notice the linearity in the ΔU^+ curve, and the slope is very close to the one predicted by Bechert et al.[5].

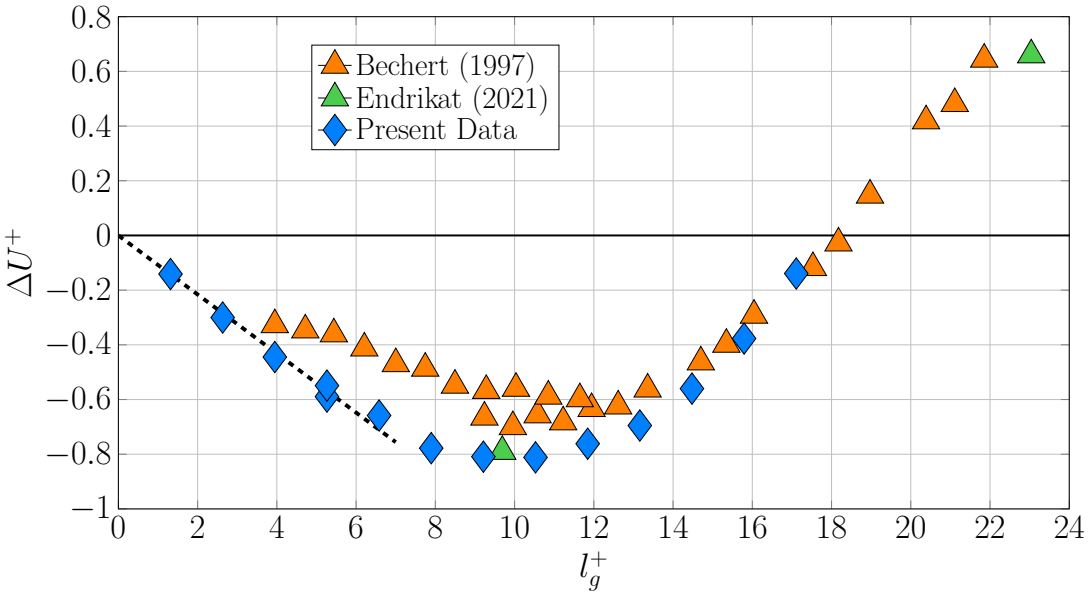

Figure 15: ΔU^+ values compared to available data for 60° tip angle straight riblets.

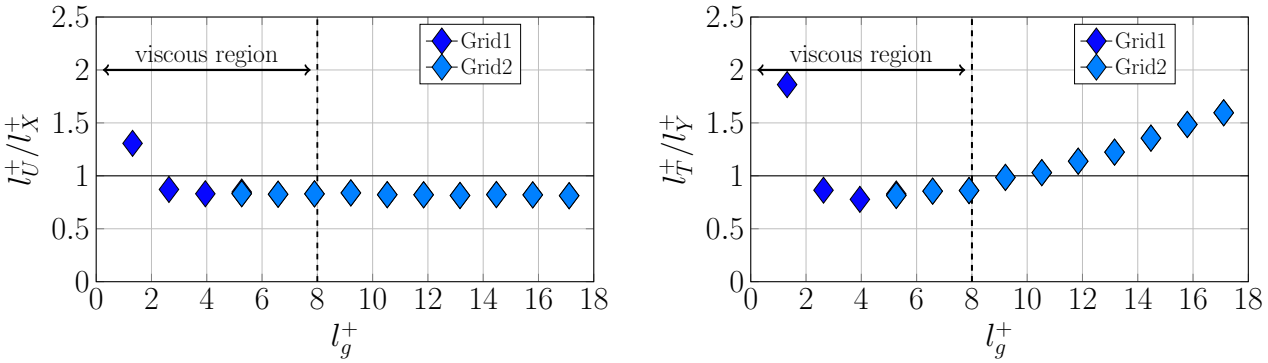

Figure 16: Scaling of mean and turbulent flow virtual origins with parallel and perpendicular protrusion heights for straight riblets.

In Figure 15 our results are compared to the ones from Endrikat et al. [10], computed with a minimal channel domain, and to the ones obtained from Bechert's $\Delta\tau\%$ values as explained in Section 4.3. It is possible to see how Endrikat's point at lower l_g^+ is very close to our dataset, while the values obtained from Bechert et al.[5]'s are a bit off, especially around the maximum-drag-reduction region, while they match pretty well at higher l_g^+; of course, the method used to extrapolate their points is questionable, as ΔU^+ values should be calculated starting from the velocity and turbulent shear stress profiles.
Starting from l_T^+ and ΔU^+ values, it is possible to calculate the virtual origin of the mean flow as $l_U^+ = -\Delta U^+ + l_T^+$. In the viscous region, the expectation is to have values for the mean and turbulent flow's virtual origins very close to the parallel and perpendicular protrusion heights l_X^+, l_Y^+ [20]. These equalities are expected to hold until $l_g^+ \simeq 8$, while for higher riblet sizes, the position of turbulence's virtual origin should depart from the perpendicular protrusion height, as considering a virtual origin for the spanwise flow only isn't sufficient

anymore to predict the correct origin for turbulence, due to second-order effects becoming non-negligible [15]. It is possible to see in Figure 20 how, apart from the smallest geometries, where uncertainty rises because of the very small values of both l_T and ΔU, l_U^+ perfectly scales with l_X^+ for all l_g^+; l_T^+, as expected, scales with l_Y^+ for riblets falling into the viscous regime and diverges from l_Y^+ values for larger l_g^+.
The evalutation of the Re_τ-independent parameter ΔU^+ is possible for sinusoidal riblets as well. Figure 17 and 18 demonstrate that, like in the case of straight riblets, the grooved surface does not modify the velocity profiles, except for the shifts in the virtual origins for the mean and turbulent flows. This remains true despite the drag-reducing mechanisms resulting from spanwise forcing control, which in general affect the universality of U^+ and $\langle uw \rangle^+$, as shown by [2]. However, the passive nature of the sinusoidal riblets control allows us to consider the surface as a type of surface roughness. Therefore, the universality of mean velocity and turbulent shear stress profiles is preserved when accounting for the correct virtual origins. This is because the spanwise motions induced by the riblets' shape are a secondary effect when compared to the virtual origin one.

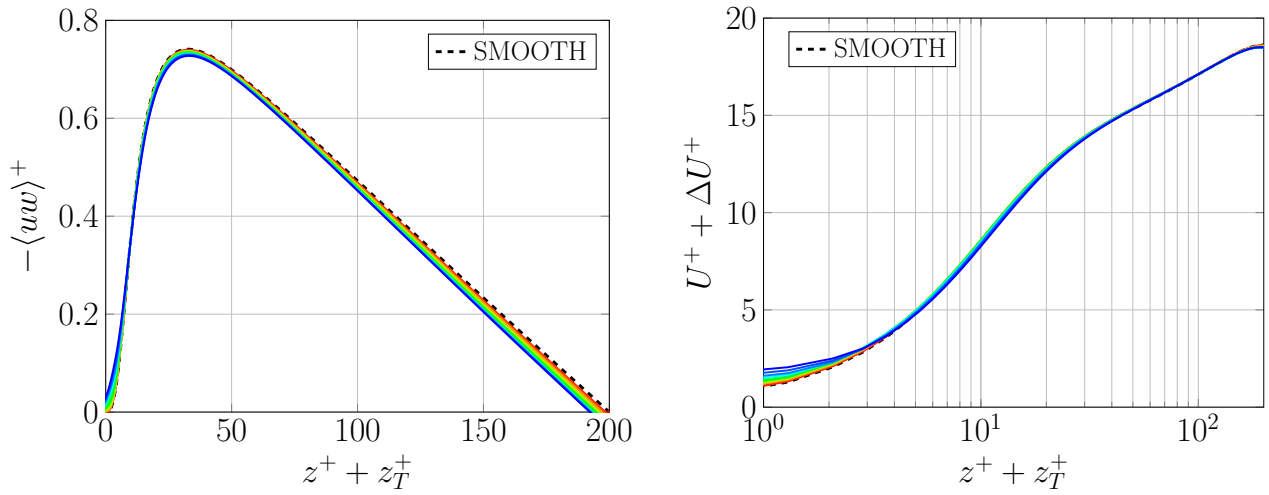

Figure 17: Rescaled Mean Velocity and Turbulent Shear Stress profiles for LONG geometry.

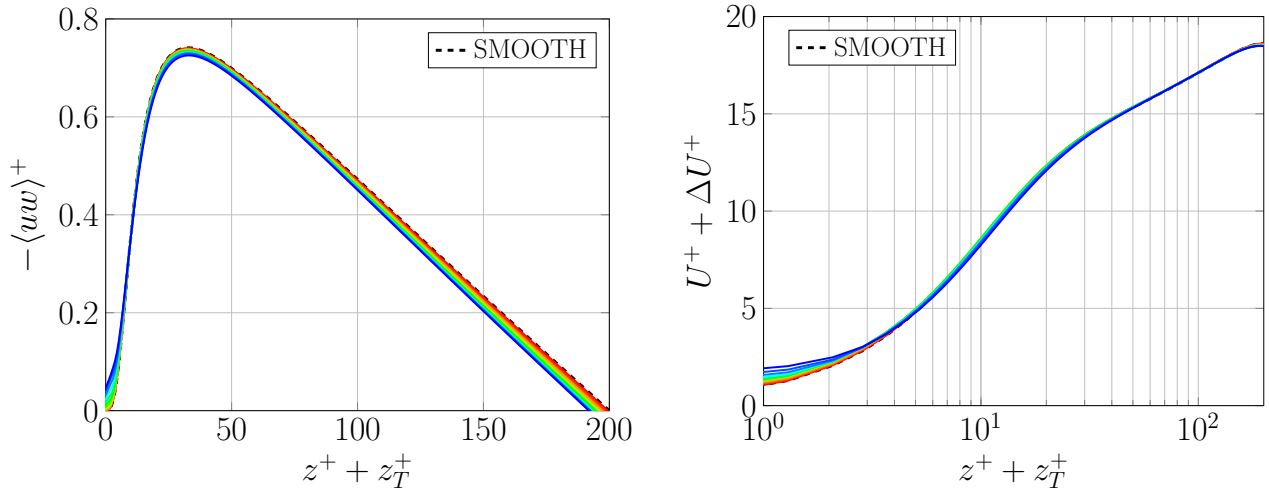

Figure 18: Rescaled Mean Velocity and Turbulent Shear Stress profiles for SHORT geometry.

In Figure 19, all three geometries are compared in terms of ΔU^+. Again, it is possible to note that the smallest riblets for sinusoidal configurations yield contradictory values compared to the viscous region prediction. This is because we can only catch a glimpse of the linearity typical of this regime, and especially the points at $l_g^+ \approx 2.5$ do not fall into this regime. Nevertheless, if we look at the slope of the linear regime, it is noticeable that the LONG geometry presents a higher viscous slope, confirming what was previously predicted in 4.1. The main remark, similarly to the $\Delta C_f\%$ plot, is that sinusoidal riblets, at least in these two configurations, yield more drag reduction than straight ones, and the LONG geometry performs better than the SHORT one.
From Figure 20, the ratios between the mean (turbulent) flow virtual origins and the streamwise (spanwise) flow virtual origins are displayed. We observe a very similar behavior compared to straight riblets, apart from some

differences in the l_T^+/l_Y^+ ratios for large riblets. It is possible to note how the similarity between l_T^+ and l_Y^+ for sinusoidal riblets is extended for larger l_g^+ compared to the straight ones. This is a symptom of the enlargement of the viscous regime provided by sinusoidal riblets. It is also visible how the displacement of the turbulent flow is lower for sinusoidal geometries, meaning that straight riblets are able, for large l_g^+, to shift turbulent structures further from the wall compared to sinusoidal riblets. This results in reduced turbulence in the near wall region. The fact that sinusoidal riblets yield higher drag reduction means that they are capable of adding a secondary mechanism to help reduce friction drag lower than their straight counterpart. This secondary mechanism is likely to be similar to the spanwise forcing mechanism, which is able to shelter the inner portion of the channel from turbulent drag increasing phenomena thanks to the spanwise shear introduced by the sinusoidal riblets geometry.

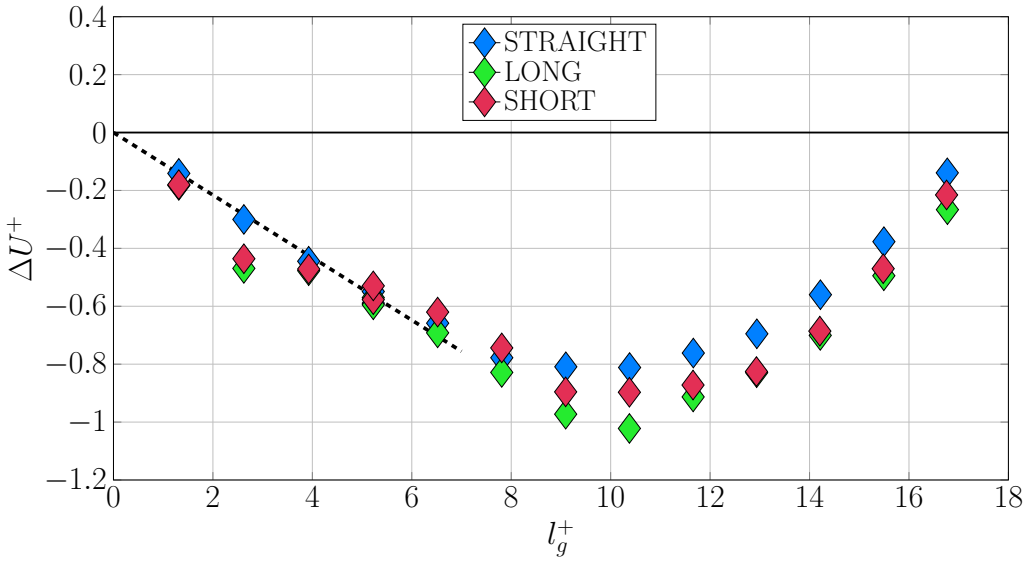

Figure 19: Plot of the Re_τ independent parameter ΔU^+ for straight and sinusoidal riblets.

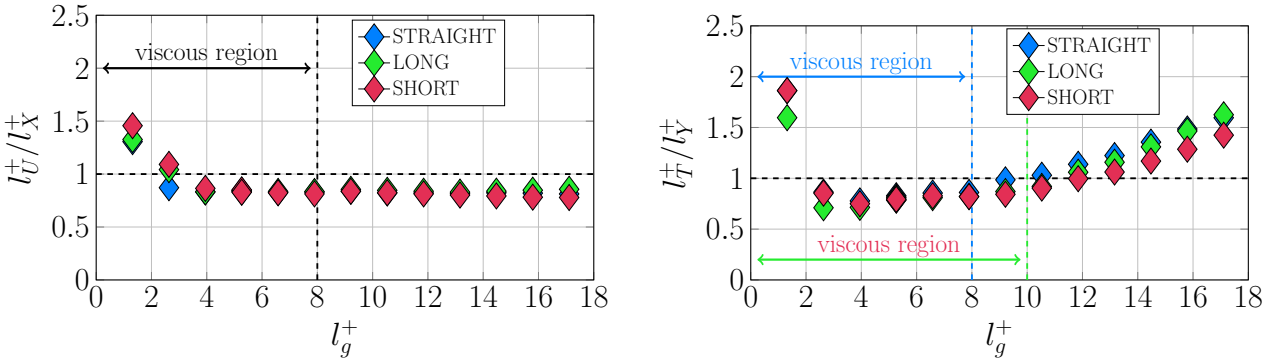

Figure 20: Scaling of mean flow and turbulent virtual origins with parallel and perpendicular protrusion heights.

4.4. Turbulent Simulations: QSV

In this last section, the position and intensity of Quasi-Streamwise-Vortices (QSVs) are studied using the "Lambda CI" algorithm. This involves selecting about 100 3D velocity fields representing the entire domain and calculating the scalar Λ at every point of the pressure grid to represent the QSV intensity at that point. Λ is nonzero only when the velocity gradient tensor at the point has complex conjugate eigenvalues $\lambda_{1,2} = \alpha \pm i\beta$. Λ is defined as $\Lambda = \beta$. This is effective because, when considering a point inside a QSV, it is likely that the product $(dv/dz)(dw/dy)$ is negative. Since the two factors lie in symmetric positions of the velocity gradient tensor, their product contributes negatively to the discriminant of the quadratic equation formula used to calculate the eigenvalues.

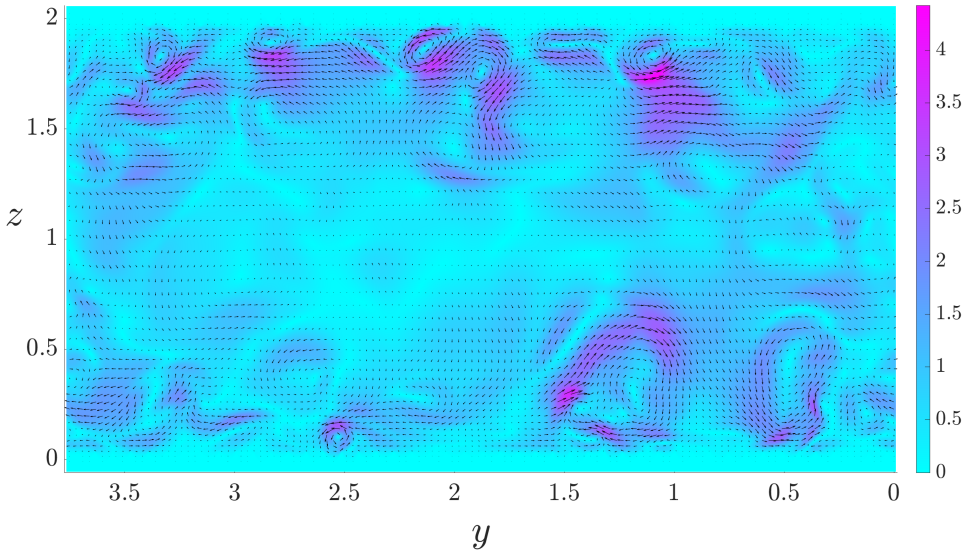

Figure 21: Screenshot of the spanwise and wall-normal velocity components on a plane orthogonal to the x-axis. The color indicates the magnitude of the velocity vectors in this plane.

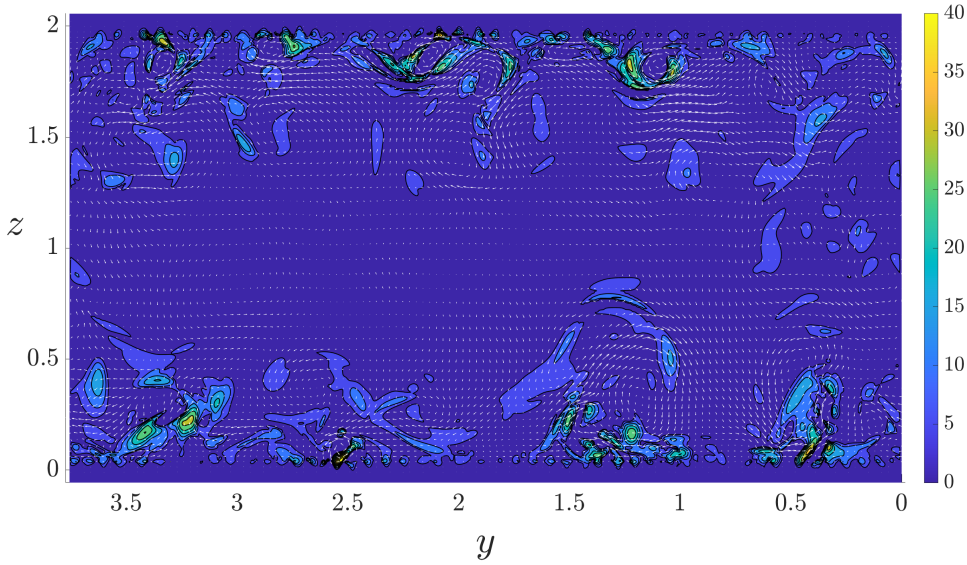

Figure 22: Screenshot of the scalar Λ on a plane orthogonal to the x-axis. The color indicates the intensity of the QSVs, that are predominantly located in the buffer layer.

An example of how the algorithm works on a plane normal to the streamwise direction is shown in Figure 21 and 22. In Figure 21, the field of the spanwise and wall-normal velocity components is plotted, while in Figure 22, the values of the scalar Λ at every pressure-grid point are plotted on the same slice. The peaks in the Λ distribution correspond to areas where the vorticity is high. Finally, these Λ-fields are averaged along the homogeneous directions and for every velocity field of the considered geometry, resulting in a function $\Lambda(z^+)$ for every riblet size. These Λ distributions for straight riblets are plotted in Figure 23.
From Figure 23 we can see how the distribution of the scalar Λ changes w.r.t. the smooth channel case. In the outer region the profiles are almost overlapping, meaning that the turbulence intensity far from the wall is unaffected by the presence of the riblets. For the smooth reference channel, the function $\Lambda(z^+)$ has a peak at $z^+ \approx 11$ in the buffer layer. As we introduce riblets in our channel and increase their size, we see how the main peak remains in the buffer layer, but its position and intensity vary with the size of riblets. Also, a secondary and more irregular peak appears at lower z^+, but this peak is fictitious, as it is due to the discontinuities in the velocity field at the riblets tips, so we will neglect it.

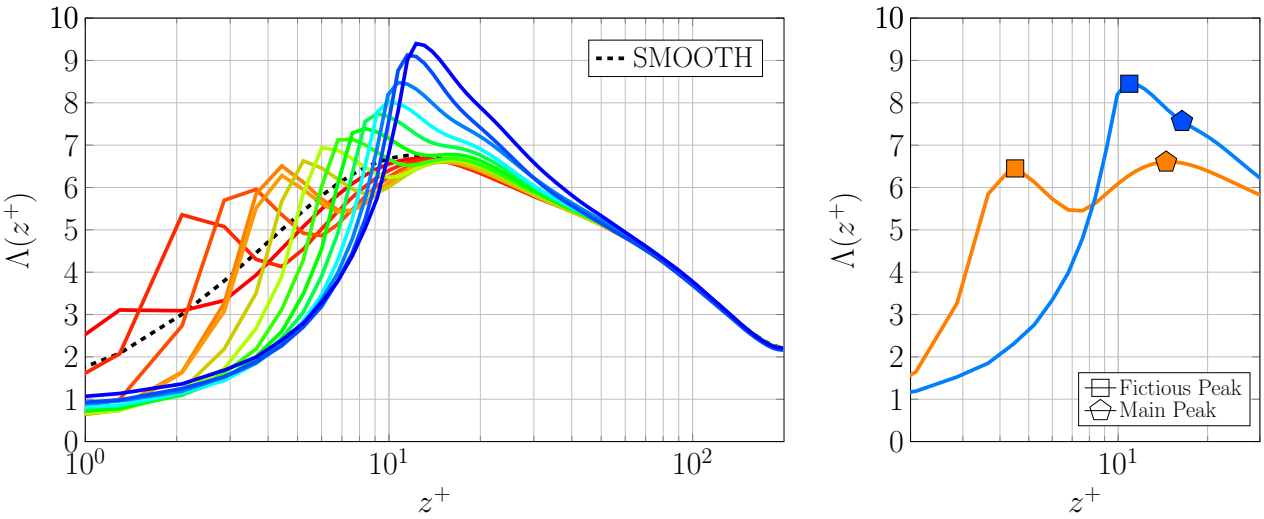

Figure 23: Averaged values of $\Lambda(z^+)$ for every riblets size for the STRAIGHT geometry. The red curve represents the smaller cross-section area geometry, the blue ones the largest one. On the right we focus on the presence of the fictious and real peaks; the main peak is taken, for the larger geometries, as the point of local minimum for the derivative of $\Lambda(z^+)$.

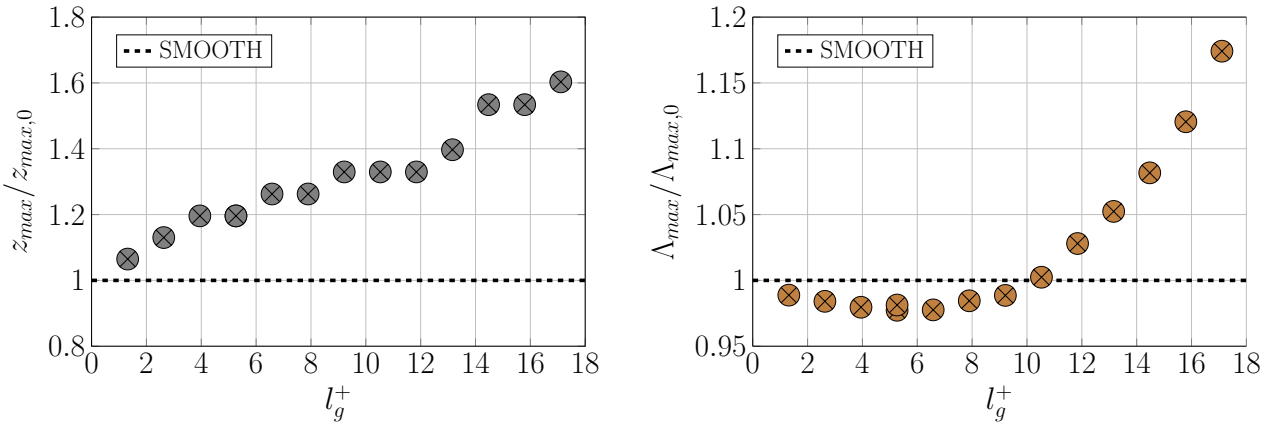

Figure 24: Position and intensity of Λ's peak compared to the smooth reference case.

It is possible to point out that, with small riblets (red curves), the peak position is slightly moved towards the half channel, and its intensity is reduced. This is the effect we were talking about in Section 1: riblets, in their drag-reducing regime, push turbulence away from the wall, reducing the strength of the wall cycle and thus reducing the turbulence level close to the wall. As we increase the riblet size, it is possible to observe how the peak position keeps moving towards the centre of the channel, but, differently from the profiles coming from geometries in the viscous regime, the magnitude of Λ at the peak rises because the drag-increasing mechanisms of riblets become predominant. In fact, when riblets become too large, their geometry induces a higher momentum mixing close to the wall, which increases the turbulence level.
This behavior is highlighted in Figure 24, where we isolate from Figure 23 only the position and magnitude of the peak and compare it to the reference ($_0$) values of the smooth channel. It is clear how the position of the peak is monotonically shifted towards the half channel, but the intensity of the peak has a different behavior: in fact, for riblets in the viscous regime, the intensity goes down below that of a smooth channel, but as we keep increasing the riblet dimension, this effect is counteracted by some drag-increasing phenomena that interestingly take over at the same l_g^+ that allows for maximum drag reduction. From that point on, the magnitude of the peak keeps growing, and the friction drag generated by the corresponding geometries increases with it (14).

5. Conclusions

In this thesis, an innovative finite-differences DNS code capable of simulating a channel flow controlled using riblets on both walls is presented. The effectiveness of the code is demonstrated by employing a riblets geometry with 60° tip angles and comparing the results to other experimental and numerical researches with the same configuration. The code's most important innovation is the corner correction, which is integrated with an implicit immersed boundary method to enable a cost-effective discretization of the domain around the riblets' tips. This area, which in other codes would require an extremely fine spatial discretization to accurately resolve the geometrical singularities in turbulent flow, is modified using the corner correction by changing the immersed boundary coefficients relative to points located in the close proximity of the edges. The aim of this correction is to enforce the steady Stokes and Laplace solutions for a wedge geometry in these areas, as very close to the tips, convective and time-evolving terms are an order of magnitude smaller compared to the other terms of the Navier Stokes equations, and can therefore be disregarded. It is shown that, in both laminar and turbulent simulations, this correction is necessary to achieve valuable results with low computational cost.
The results presented in this paper are in good agreement with previous experimental and numerical studies such as Bechert et al. [5], Endrikat et al. [10] for the same geometry. The only discrepancies observed are due to the low Reynolds number of the simulations, which can be augmented with little impact on computational costs. The findings confirm that straight riblets with a 60° tip angle can generate a maximum drag reduction of 5% in their optimal configuration and an upward shift in the mean velocity profile of around 0.81 plus units. More theoretical studies, such as the implementation of the Λ_{CI} algorithm to investigate turbulent structures, further confirm the existing literature on the functioning of riblets: up until a certain cross-section area, riblets reduce the intensity of near-wall turbulence and are able to move turbulent structures away from the wall monotonically with l_g^+.
The secondary objective of the thesis was to evaluate the effectiveness the sinusoidal riblets, at least in two of the possible configurations. The results proved that this configurations can enhance riblets performance thanks to the spanwise motions they induce to the near wall flow typical of spanwise forcing control, with the LONG geometry able to increase by 29% the maximum drag reduction generated by classical straight riblets. The fact that only 2 points in the λ_x^+ - β_{max} plane were simulated leaves room for potential improvements in the maximum achievable drag reduction. It is our belief that this cost-efficient code can enable broad parametric studies in the future. Emphasis will also be placed on improving the accuracy of our results for the viscous region, wherein the code is insufficiently adept at capturing the precise amount of drag reduction achieved by sinusoidal riblets at extremely low l_g^+.
Thanks to the generality of the implementation, these studies can easily be extended to other geometries, such as other tip angles or other cross-section shapes, including trapezoidal or parabolic riblets, as reported in Bechert et al. [5]. They can also be extended to any desired geometry that has a sharp tip angle, since the only required information is the steady Laplace/Stokes solution for the considered geometry, which is, at worst numerically, always available.

References

[1] Adel Abbas, Gabriel Bugeda, Esteban Ferrer, Song Fu, Jacques Periaux, Jordi Pons-Prats, Eusebio Valero, and Yao Zheng. Drag reduction via turbulent boundary layer flow control. *Science China Technological Sciences*, 60(9):1281–1290, September 2017.

[2] A. Baron and M. Quadrio. Turbulent drag reduction by spanwise wall oscillations. *Applied Scientific Research*, 55:311–326, 1996.

[3] D. Bechert and W Reif. On the Drag Reduction of the Shark Skin. In *23rd Aerospace Sciences Meeting*, number 1 in Aerospace Sciences Meetings. American Institute of Aeronautics and Astronautics, January 1985.

[4] D.W. Bechert, M. Bruse, and W. Hage. Experiments with three-dimensional riblets as an idealized model of shark skin. *Experiments in Fluids*, 28:403–412, 2000.

[5] D.W. Bechert, M. Bruse, W. Hage, J.G.T. Van Der Hoeven, and G. Hoppe. Experiments on drag-reducing surfaces and their optimization with an adjustable geometry. *Journal of Fluid Mechanics*, 338:59–87, 1997.

[6] L. Cacciatori, C. Brignoli, B. Mele, F. Gattere, C.M. Monti, and M. Quadrio. Drag Reduction by Riblets on a Commercial UAV. *Appl. Sci.*, 12(10):5070, 2022.

[7] Gioacchino Cafiero and Gaetano Iuso. Drag reduction in a turbulent boundary layer with sinusoidal riblets. *Experimental Thermal and Fluid Science*, 139:110723, November 2022.

[8] H. Choi, P. Moin, and J. Kim. Direct numerical simulation of turbulent flow over riblets. *J Fluid Mechanics*, 255:503–539, October 1993.

[9] S. Endrikat, D. Modesti, R. García-Mayoral, N. Hutchins, and D. Chung. Influence of riblet shapes on the occurrence of Kelvin–Helmholtz rollers. *Journal of Fluid Mechanics*, 913, April 2021.

[10] S. Endrikat, D. Modesti, M. MacDonald, R. García-Mayoral, N. Hutchins, and D. Chung. Direct Numerical Simulations of Turbulent Flow Over Various Riblet Shapes in Minimal-Span Channels. *Flow, Turbulence and Combustion*, 107(1):1–29, June 2021.

[11] R. Garcia-Mayoral and J. Jiménez. Hydrodynamic stability and the breakdown of the viscous regime over riblets. *J. Fluid. Mech.*, 678:317–347, 2011.

[12] Gatti, von Deyn, Forooghi, and Frohnapfel. Do riblets exhibit fully rough behaviour? *Experiments in Fluids*, 61(3):81, March 2020.

[13] D. Gatti and M. Quadrio. Reynolds-number dependence of turbulent skin-friction drag reduction induced by spanwise forcing. *J. Fluid Mech.*, 802:553–58, 2016.

[14] D. Goldstein and T. Tuan. Secondary flow induced by riblets. *J Fluid Mechanics*, 363:115–151, 1998.

[15] J. I. Ibrahim, G. Gomez-de-Segura, D. Chung, and R. Garcia-Mayoral. The smooth-wall-like behaviour of turbulence over drag-altering surfaces: A unifying virtual-origin framework. *Journal of Fluid Mechanics*, 915:A56, 2021.

[16] J. Jimenez. On the structure and control of near wall turbulence. *Phys. Fluids*, 6:944–953, 1994.

[17] P. Luchini. Linearized no-slip boundary conditions at a rough surface. *J. Fluid Mech.*, 737:349–367, 2013.

[18] P. Luchini. Immersed-boundary simulation of turbulent flow past a sinusoidally undulated river bottom. *Eur. J. Mech. B / Fluids*, 55:340–347, 2016.

[19] P. Luchini. Introducing CPL. *2012.12143*, November 2021.

[20] P. Luchini, F. Manzo, and A. Pozzi. Resistance of a grooved surface to parallel flow and cross-flow. *Journal of Fluid Mechanics*, 228:87–109, 1991.

[21] B. Mele, R. Tognaccini, and P. Catalano. Performance assessment of a transonic wing-body configuration with riblets installed. *J. Aircr.*, 53(1):129–140, 2016.

[22] Y. Peet, P. Sagaut, and Y. Charron. Turbulent Drag Reduction using Sinusoidal Riblets with Triangular Cross-Section. *AIAA Paper 2008-3745*, June 2008.

[23] M. Quadrio, B. Frohnapfel, and Y. Hasegawa. Does the choice of the forcing term affect flow statistics in DNS of turbulent channel flow? *Eur. J. Mech. B / Fluids*, 55:286–293, 2016.

[24] M. Quadrio, P. Ricco, and C. Viotti. Streamwise-traveling waves of spanwise wall velocity for turbulent drag reduction. *Journal of Fluid Mechanics*, 627:161–178, 2009.

[25] M. Sasamori, O. Iihama, H. Mamori, K. Iwamoto, and A. Murata. Parametric Study on a Sinusoidal Riblet for Drag Reduction by Direct Numerical Simulation. *Flow, Turbulence and Combustion*, 99(1):47–69, 2017.

[26] M Sasamori, H. Mamori, K. Iwamoto, and A. Murata. Experimental study on drag-reduction effect due to sinusoidal riblets in turbulent channel flow | SpringerLink. *Experiments in Fluids*, 55, April 2014.

[27] Lars H. von Deyn, Davide Gatti, and Bettina Frohnapfel. From drag-reducing riblets to drag-increasing ridges. *J Fluid Mechanics*, 951:A16, November 2022.

[28] M. J. Walsh and L. M. Weinstein. Drag and Heat-Transfer Characteristics of Small Longitudinally Ribbed Surfaces. *AIAA Journal*, 17(7):770–771, 1979.

Abstract in lingua italiana

Nella presente tesi viene presentato un codice di simulazione numerica diretta (DNS) a differenze finite progettato per valutare la riduzione della resistenza di attrito turbolento generata da riblets di forma arbitraria. Il punto di forza del codice risiede nella sua efficienza, ottenuta mediante l'implementazione di un metodo ai contorni immersi che incorpora una correzione dello spigolo per le punte delle riblets. L'idea si basa sull'osservazione che, nei pressi delle singolarità geometriche, i termini convettivi sono trascurabili: la soluzione stazionaria analitica del problema di Stokes viene utilizzata per correggere i termini Immersed Boundary. Di conseguenza, non sono necessarie mesh estremamente fini per risolvere correttamente la punta delle riblets. L'efficienza computazionale del codice ha permesso un'analisi parametrica della geometria delle riblets, in particolare sono state testate riblets triangolari con angolo di 60 gradi dirette in direzione del flusso medio per un'ampia gamma di dimensioni delle riblets al fine di misurare la curva di drag reduction. La Corner Correction è risultata cruciale per la corretta simulazione di correnti laminari e turbolente. I risultati sono illustrati in termini di coefficiente di attrito e shift del profilo di velocità medio. Vengono inoltre presentate alcune statistiche della turbolenza, come gli sforzi di Reynolds, i profili di velocità media e la posizione e intensità dei Quasi-Stramwise-Vortices. Un focus particolare viene rivolto all'efficienza delle riblets sinusoidali rispetto alla configuarazione rettilinea.

Parole chiave: Turbolenza, Attrito, Riblets, Navier-Stokes, DNS, Immersed Boundary, CPL

Acknowledgements

Colgo l'occasione per ringraziare di cuore tutta la mia famiglia e i miei amici che mi hanno sempre accompagnato in questi anni di studio e hanno sempre creduto in me anche nei momenti più difficili.
Un pensiero particolare va a Davide, che mi ha accompagnato in questo percorso di tesi, lo ringrazio per i numerosi insegnamenti ricevuti e per la grandissima disponibilità che ha sempre dimostrato nei miei confronti. Infine, un grazie al Prof. Maurizio Quadrio e all'Ing. Federica Gattere, per avermi dato la possibilità di concludere i miei studi con questo lavoro di tesi e per avermi sempre sostenuto durante questi mesi.

Stefano